CrossMark

# Thermal Modeling of Al-Al and Al-Steel Friction Stir Spot Welding

P. Jedrasiak, H.R. Shercliff, A. Reilly, G.J. McShane, Y.C. Chen, L. Wang, J. Robson, and P. Prangnell

This paper presents a finite element thermal model for similar and dissimilar alloy friction stir spot welding (FSSW). The model is calibrated and validated using instrumented lap joints in Al-Al and Al-Fe automotive sheet alloys. The model successfully predicts the thermal histories for a range of process conditions. The resulting temperature histories are used to predict the growth of intermetallic phases at the interface in Al-Fe welds. Temperature predictions were used to study the evolution of hardness of a precipitation-hardened aluminum alloy during post-weld aging after FSSW.

## 1. Introduction

Redesign of the vehicle body in lightweight materials remains a key strategy in the challenge to improve fuel efficiency and to reduce carbon dioxide and other emissions. This requires innovation in cost-effective joining technologies, while meeting the technical demands for crashworthiness and stiffness of the vehicle structure. By avoiding melting, friction welding methods avoid many metallurgical problems associated with fusion processes, particularly for joining aluminum, magnesium, high strength steels, and also dissimilar material combinations.

Friction stir spot welding (FSSW) is regarded as a potential alternative to resistance spot welding and self-piercing riveting, the conventional joining processes for automotive sheet materials (Ref 1). A rotating cylindrical tool, made from a hard and wear-resistant material, is pressed against two overlapping sheets. The tool may feature a specifically designed pin, protruding from the tool shoulder. Frictional and deformation heating softens the material, and the tool is retracted after a plunge and dwell time of the order of 1 s (Fig. 1). In previous work, Prangnell and co-workers (Ref 2-6) produced sound joints with a pinless tool, without the need for mechanical interlocking associated with a pin penetrating the bottom sheet. This eliminated the residual hole formed by a conventional tool, which reduces the effective joint area and can lead to corrosion (Ref 7). It also shortened the cycle time compared to conventional and refill FSSW, which is desirable for automotive production.

Gerlich and co-workers provide evidence of the material state and temperature in FSSW of Al and Mg alloys (Ref 8-13). Melting was apparent beneath the pin in some conditions, reflecting the larger contact time and pressure under the pin during the plunge, but the temperature below the shoulder was up to 45 K lower than below the pin. For the rotational speed and dwell times used in the present study, without a pin, their work suggests a maximum temperature well below the solidus temperature (Ref 10). To achieve a sound joint in solid-sate FSSW, the oxide layers must be broken up by sufficiently large deformation to give metal-metal bonding at the interface (Ref 14, 15). For the temperatures and strain rates in FSSW, diffusion processes at the interface in dissimilar joints may lead to the formation of intermetallic compounds, which influence the performance of the joint.

A number of authors have developed thermomechanically coupled models of FSSW using computational fluid dynamics (Ref 16-20), the meshless particle method (Ref 21), or the finite element method (Ref 22-24). To handle the severe non-steady-state deformations, computational schemes include Lagrangian (Ref 25, 26) or arbitrary Lagrangian-Eulerian (ALE) (Ref 27-29) kinematic descriptions, and explicit time integration (Ref 27-31). While coupled models can provide insight into material flow and heat generation, these approaches are computationally expensive, for example, due to the extensive remeshing required, making detailed parametric or optimization studies time-consuming (Ref 30). Furthermore, some of these studies also lack any experimental validation, or only deal with the initial tool plunge.

This paper presents a thermal-only implicit FE model of pinless FSSW, allowing time-efficient parametric studies and reverse engineering of heat generation. Most FSSW modelers assume either sticking at the interface (Ref 16, 18), or a Coulomb friction law with a constant (Ref 21-23, 26-28, 31) or temperature-dependent coefficient of friction (Ref 24, 29, 30). With few exceptions (Ref 20, 28), no independent machine torque or power measurements have been provided to validate the assumed contact model. In the present work, a spatial power distribution based on a stick-slip condition at the tool-workpiece interface is adopted, informed by kinematic and microstructural studies of FSSW in dissimilar Al alloys (Ref 32). Multiple thermocouple measurements are used to calibrate the net power as a function of time, to provide a predictive capability for microstructural modeling.

**P. Jedrasiak, H.R. Shercliff, A. Reilly,** and **G.J. McShane**, Department of Engineering, University of Cambridge, Trumpington St, Cambridge CB2 1PZ, UK; and **Y.C. Chen, L. Wang, J. Robson,** and **P. Prangnell**, Materials Science Centre, University of Manchester, Grosvenor St, Manchester M1 7HS, UK. Contact e-mail: hrs@eng.cam.ac.uk.

## 2. Experimental Work

Instrumented welds were produced in two standard automotive sheet materials: 6111-T4 Al alloy (0.93-mm thick) welded to itself, and to ungalvanized mild steel DC04 (0.97-mm thick). Figure 2 shows the two tool designs used, both 10 mm in diameter and manufactured from H13 tool steel: a flat featureless tool and a tool with flutes machined into the shoulder. The welding conditions were selected from a wider matrix of trials, to give joints with acceptable shear strength and failure energy, failing by nugget pull-out rather than debonding. Welding was done under position control on a CS Powerstir FSW machine, with the parameters as shown in Table 1.

The workpiece clamping arrangement is presented in the FE model below. In Al-Al welds, temperature was measured by K-type thermocouples embedded in the steel anvil at radial distances of 2.5, 5, and 10 mm from the tool center. The thermocouple tips projected ∼0.1 mm above the anvil ensure good contact. In Al-steel welds, K-type thermocouples were embedded 0.1 mm beneath the Al-steel interface, at the tool center, and at a radial distance of 2.5 mm. The repeatability of the thermal cycles was principally limited by the accuracy of locating the thermocouples, but was estimated to be better than 10 °C (by comparing data between welds in nominally identical welds). Machine torque was recorded to indicate the overall shape of the power input history, but at too low a level of accuracy for modeling purposes, due to a high idling torque and machine losses.

To determine the nature and thickness of the intermetallic layer, cross-sections of the weld were prepared by sectioning through the center of the welds. Specimens were prepared for metallographic examination following standard grinding and polishing procedures. Weld cross-sections were then examined using a field emission gun scanning electron microscope (FEI Magellan FEGSEM) operated at 20 kV. Backscattered imaging mode was used to clearly identify both parent materials and the intermetallic reaction layer. Example images are presented elsewhere (Ref 3, 33). The intermetallic layer is not uniform in thickness, but shows considerable local fluctuations (see Ref 3, 33). Measurement points were defined with a spacing of approximately 0.6 mm across the weld. To determine a reliable average intermetallic layer thickness, the total area occupied by intermetallic was measured in a region bound by positions midway between measurement points (i.e., ±0.3 mm from the measurement point). This area was divided by the measurement distance (0.6 mm) to give an average intermetallic thickness at that measurement point. In this way, local fluctuations in the layer thickness are smoothed out, while still allowing the change in average layer thickness across the weld to be reliably tracked.

Microhardness profiles were measured on sections through the center of the welds, at mid-thickness of the top sheet. Measurements were made immediately after welding (<1 h), after 3 months of natural aging, and following a simulated paint-bake thermal cycle (artificial aging at 180 °C for 30 min immediately after welding).

## 3. Finite Element Modeling

### 3.1 Geometry and Materials

Figure 3 shows the dimensions and mesh of the 3D finite element model, including workpieces, tool, backing plate, and a top clamping plate. As there are two planes of symmetry, it was only necessary to model one quarter of the entire assembly, decreasing calculation time. The mesh consisted of about 5000 elements, with the backing plate being meshed with tetrahedral elements, to allow greater variation of element size within the part, improving computational efficiency. A simplified, fast axisymmetric model was used first to optimize the minimum mesh size (0.3 mm) and the computational time step (0.1 s).

All material properties in the model were temperature-dependent. Density, thermal conductivity, and specific heat of AA6111 were available as a function of temperature (Ref 34).
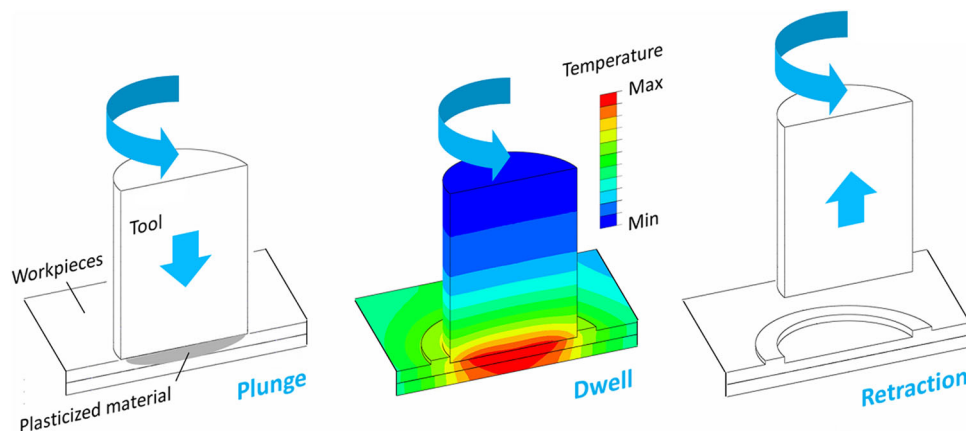


**Fig. 2** Tool designs



**Fig. 1** Schematic of pinless friction stir spot welding of a lap joint

**Table 1  Experimental Conditions for Al-Al and Al-Fe Friction Stir Spot Welds**

| Weld number | I | II | III | IV |
|---|---|---|---|---|
| Top sheet material | 6111-T4 Al | 6111-T4 Al | 6111-T4 Al | 6111-T4 Al |
| Bottom sheet material | 6111-T4 Al | 6111-T4 Al | DC04 steel | DC04 steel |
| Tool type | Flat | Fluted | Flat | Fluted |
| Plunge-rate, mm/min | 150 | 150 | 100 | 100 |
| Retraction-rate, mm/min | 150 | 150 | 50 | 50 |
| Plunge depth, mm | 0.2 | 0.2 | 0.3 | 0.3 |
| Rotational speed, rpm | 2000 | 2000 | 2000 | 2000 |
| Dwell time, s | 2.5 | 2.5 | 1 | 1 |
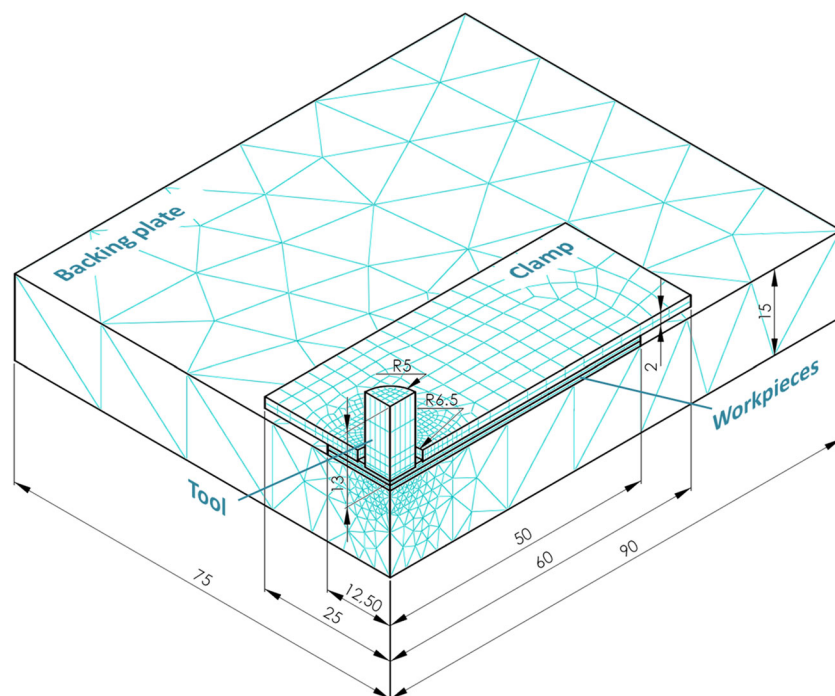


**Fig. 3**  Thermal FE model of FSSW: weld layout, dimensions (in mm), and mesh

For the various steel grades, properties were selected for the similar alloys shown in brackets: DC04 (low carbon steel) (Ref 35); H13 (Ref 36); 4340 (Ref 37).

The plunge stage presents a particular problem in modeling FSSW, since the thermal model required the tool location and associated heat input to be fixed. In reality, some unknown proportion of the weld time is used reaching the maximum depth (of order 1 s), as the material needs to be softened for the tool to penetrate the surface. A preliminary sensitivity analysis was conducted to test the effect of the plunge depth on the predicted thermal field at the weld interface, and it was found to be of secondary importance for plunge depths up to half the thickness of the top 1-mm thick sheet. The model plunge depth was therefore set to be equal to the final depth: 0.2 mm in Al-Al welds, and 0.3 mm in Al-Fe welds. Flash was included in the model in the anular gap between the tool and the top clamp, with the height of the flash being calculated to conserve the volume of workpiece material.

### 3.2  Thermal Boundary Conditions

All the surfaces in contact with the air were treated as insulated, justified by the low heat transfer to air, and the short FSSW cycle time (1-5 s). Different metal-to-metal contacts had specified interface conductances, as shown in Fig. 4 and Table 2. Between the top workpiece and both tool and lower workpiece, the high pressure and applied shear give intimate metal-metal contact, so perfect thermal contact was assumed. Elsewhere, the contact conductance depends on the contact pressure. As the tool plunges, the contact pressure between workpiece and anvil is greatest directly under the tool. Under the clamps, and also under the tool during retraction, the pressure is orders of magnitude lower. Values for contact conductance of 5000 and 1000 $W/m^2$ K were taken from the literature, for high and low pressure contacts, respectively (Ref 38).

### 3.3  Numerical Problem in ABAQUS

After the dwell period, the tool is retracted and thermal contact between the tool and workpiece is lost. Initially, this was modeled in Abaqus by imposing step changes in heat input (to zero) and thermal conductance (to a very low value). This was found to lead to significant numerical stability problems, with the solution after the step change imposing heat flow from workpiece to tool *against* the temperature gradient—clearly a non-physical result. The problem was solved by imposing a
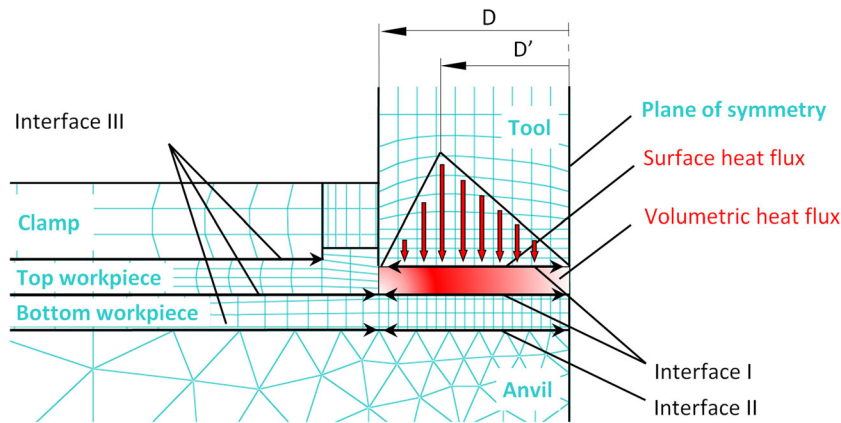
**Fig. 4** Thermal loads, metal-metal interfaces, and thermal contact conditions in the FE models of FSSW

**Table 2  Summary of Thermal Contact Conditions**

| Interface number (Fig. 4) | Contact conditions | Thermal conductance |
|---|---|---|
| I | Plasticized material | Perfect thermal contact |
| II (plunge and dwell) | High pressure, ~50 MPa | 5000, W/m$^2$K |
| II (retraction), III | Low pressure | 1000, W/m$^2$K |
| Other | Convection and radiation negligible | Insulated |

ramp change in contact conductance over several computational steps beyond the end of the dwell (for a time of order 0.1 s). This may be a more physical representation of the springback and backlash in the machine as the tool is withdrawn, but the issue highlights the unexpected numerical issues that can occur in Abaqus.

### 3.4 Thermal Loads and Calibration

The thermal FE model requires calibration of the spatial and temporal variation in the heat input. This was conducted iteratively using thermocouple data, testing the sensitivity of the predicted temperature history to the following parameters: radial distribution of heat input, the proportions of heat generated at the tool-workpiece interface and in the bulk, and the net power (as a function of time).

**3.4.1 Spatial Variation in Heat Input.** Recent work by Reilly et al. (Ref 32) has given new insight into the deformation field and heat generation during FSSW. They propose that in the central region of the tool, the material surface velocity increases proportionally with radius, representing sticking contact. However, it must reach a maximum value and fall to zero close to the tool edge, for continuity with the surrounding stationary material. This gives slip over some outer anular portion of the contact, with frictional heat generation restricted to this region, superimposed on volumetric plastic dissipation under the whole contact area. It is difficult to distinguish between surface heating and volumetric heating, particularly in thin workpieces, so the proportions of each in the model were made adjustable between 0 and 100%. As expected, the peak temperature variation with position was found to be largely independent of the proportions assumed, so a simple 50% surface/50% bulk distribution was assumed. Similarly, the volumetric heat input was assumed to extend uniformly through

the thickness of the top workpiece, as the through-thickness distribution was also found to have little influence on the peak temperature distribution at the interface.

As the workpieces are thin, the temperature field proves to be much more sensitive to the radial variation of the heat input. Since the local shear strain rate is closely related to the heat input, it is reasonable to assume that the radial distribution of the power input will reflect the surface velocity profile. For a flat tool, Reilly et al. (Ref 39) adopted a triangular surface velocity profile, so this is assumed for the radial variation of the power density, with a peak at radius $D$, expressed as a fraction of the tool radius $D'$ (Fig. 4). Reilly et al. (Ref 39) also showed via microstructural cross-sections that the tool design affects the material flow behavior. Welds created with a fluted tool consistently showed more intensive deformation associated with the fluted part of the tool groves closer to the weld center. A key calibration step in the FE simulations was therefore to assign appropriate $D/D'$ values for flat and fluted tools. These were adjusted to be 0.75 and 0.3, for flat and fluted tools, respectively. The same distribution was used for similar and dissimilar welds, as the tool-workpiece contact is assumed to be only weakly dependent on the material in the bottom workpiece.

**3.4.2 Temporal Variation in Heat Input.** The time variation of the heat generation rate $q(t)$ was adjusted empirically for the longest duration weld for each combination of materials and tools. This is a pragmatic solution to develop a working thermal model, in the absence of independent measurement of machine torque. The value of $q(t)$ was adjusted in piecewise linear fashion at 0.1-s intervals to give a good fit to the thermocouple data. An iterative implementation was used: (i) a forward prediction of the temperature change was made using the current instantaneous value of $q$ and (ii) the power in that time step was rescaled according to

the magnitudes of the experimental and predicted temperatures. The value of $q(t)$ ramped down to zero on a timescale comparable to the nominal weld time. The $q(t)$ profile was then fitted to a suitable three-part function as follows:

(i) for the plunge, a linear rise from zero to a maximum at a representative fixed value of 0.3 s;
(ii) for the dwell, an exponential decay toward a steady-state plateau value, reflecting material softening as the temperature rises. The best fit was found with the equation: $q(t) = a \cdot e^{\frac{-t+0.3}{\tau}} + b$, where $a$, $b$, and $\tau$ are calibration constants; and
(iii) for the tool retraction, a 0.5 s linear taper in heat input to zero.

Figure 5 shows the calibrated $q(t)$ for the four combinations of workpieces and tools. Three were found to coincide closely, with only the fluted tool applied to Al-steel welds requiring a modest reduction in heat input. The shape of the profile is compatible with that of the machine torque, but this was too noisy and inconsistent to be used as an input to the model.

## 4. Validation of the Fe Model

The predictive capability of the thermal model was tested by comparing with the thermocouple data for welds of varying durations. Figure 6 shows the data and predictions for 1 s Al 6111—DC04 welds, for thermocouples embedded 0.1 mm beneath the joint interface, at the tool center, and a radial distance of 2.5 mm (i.e., 0 and 0.5 times the tool radius). The cooling curve is predicted well in all cases, and the model discrepancy is within the experimental reproducibility.

Figure 7 shows the data and predictions for Al 6111-Al 6111 welds, for locations on the lower face of the lower workpiece, at radial distances of 2.5, 5, and 10 mm from the tool center (i.e., 0.5, 1, and 2 times the tool radius). The shape of the curves is reproduced well, but there are discrepancies of 10-15 °C in the peak temperatures (underpredicted at the center, and overpredicted at and beyond the tool periphery). In these welds, the thermocouples are located further from the area of heat generation, close to the workpiece-anvil interface. This gives greater sensitivity to values of the contact conductances at that interface.
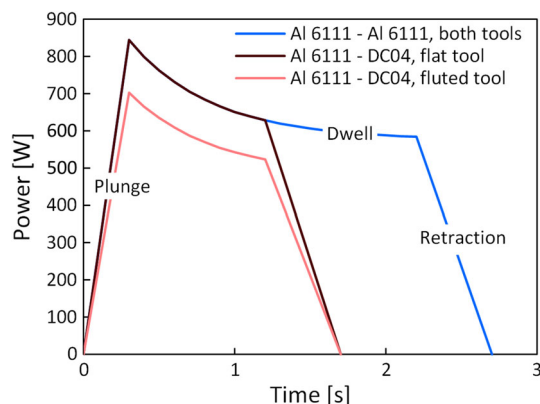
**Fig. 5** Calibrated net heat generation rate $q(t)$ for the different tools and material combinations

A comparison of the predicted temperature distributions at the weld plane of symmetry is presented in Fig. 8. Thermal maps are plotted on the same temperature scales at 1 and 2.5 s, which were the maximum welding times for Al 6111-DC04 steel and Al 6111-Al 6111 welds, respectively. Note that in all cases the predicted temperature at the center was higher for the fluted tool than for the flat tool, while the heat generated was similar, or even lower (Fig. 5). The concentration of higher temperature toward the center reflects the relative positions of the peak in the heat input ($D/D' = 0.75$ for the flat tool and $D/D' = 0.3$ for the fluted tool).

## 5. Prediction of Intermetallic Growth at Interface in Al-Fe Weld

In dissimilar solid-state welding, interdiffusion of aluminum and iron at the interface (Ref 40) leads to a driving force for nucleation and growth of intermetallic compounds (IMC). These tend to be brittle, but must form to some optimum thickness to obtain a strong metal-metal joint. Studies have shown that increasing the thickness of this intermetallic layer
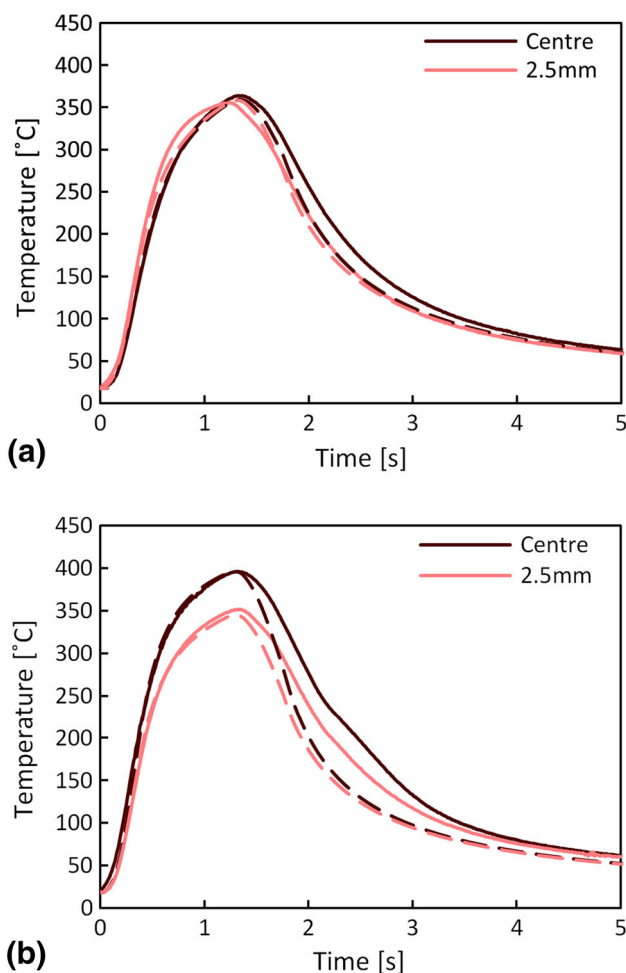
**Fig. 6** Predicted (dashed) and measured (solid) temperature histories for Al6111-DC04 steel welds, at the joint interface, for radial positions of 0 and 2.5 mm from the center: (a) flat tool; (b) fluted tool

degrades the strength of Al-steel welds made with FSSW (Ref 41) and rotary friction welding (Ref 42-45). However, a very thin IMC layer was also associated with poor mechanical properties, indicating that the welding time was insufficient to obtain a strong joint (Ref 41-43, 46).
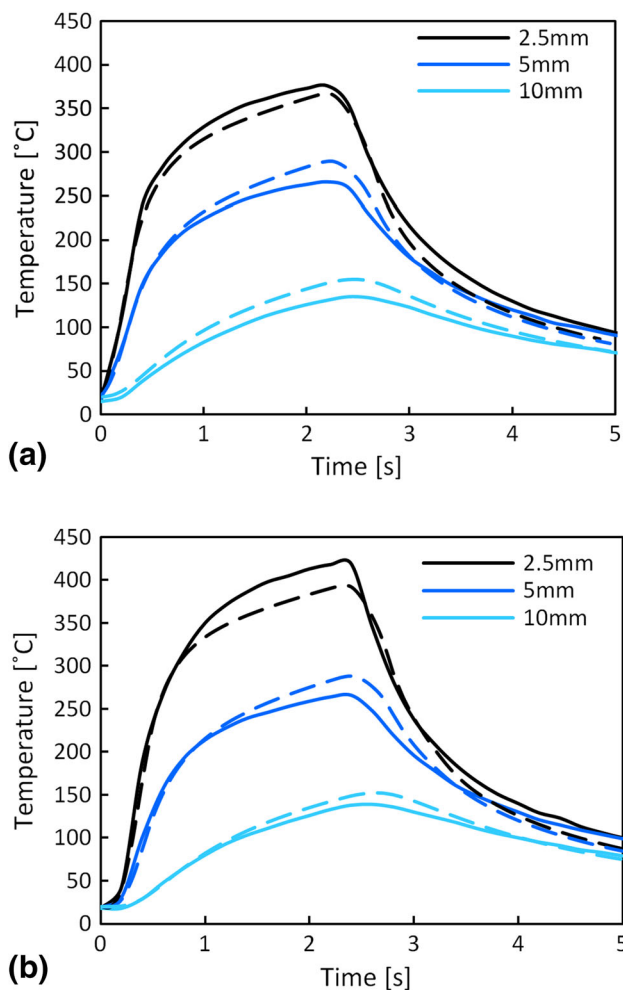


**(a)**



**(b)**

**Fig. 7** Predicted (dashed) and measured (solid) temperature histories for Al6111-Al6111 welds, at the workpiece-anvil interface, for radial positions of 2.5, 5, and 10 mm from the center: (a) flat tool; (b) fluted tool

Studies at the University of Manchester have recently characterized the formation and growth kinetics of IMC as a function of temperature during solid-state welding between Al and other metals (e.g., steels and Mg alloys), and a model has also been developed to predict the growth kinetics of IMC (Ref 1, 47, 48). For IMC growth in Al-steel FSSW, there is a short incubation time for nucleation, after which the nuclei spread over the interface, and then thicken more slowly normal to the interface. The IMC can be formed from one or two phases depending on the welding parameters. A full model for these stages is under development, but the overall layer thickness can be approximately estimated using a simple parabolic relationship, for the 1D growth rate of the layer normal to the interface:

$$\frac{dx}{dt} = kt^{-0.5}, \qquad (\text{Eq 1})$$

where $x$ is the thickness of IMC, $t$ is the welding time, and $k$ is a growth constant, which is a function of temperature described by a typical Arrhenius relationship:

$$k = k_0 e^{\left(\frac{-Q}{RT}\right)}, \qquad (\text{Eq 2})$$

where $k_0$ is the pre-exponent factor which is not affected by temperature, $Q$ is the activation energy, $R$ is the gas constant, and $T$ is the temperature in K. The growth constant parameters were obtained from Springer (Ref 49) and Kajihara (Ref 50).

The final layer thickness is determined by numerically integrating Eq 1 over the weld thermal cycle, using the value for the growth constant that corresponds to the instantaneous temperature at that integration point. Further justification of this simple approach for predicting the intermetallic layer thickness for the joint combination studied in this work (but using measured thermal profiles) is presented elsewhere (Ref 3, 33).

This model has been applied to the thermal cycles predicted across the interface in a 1 s weld between Al 6111 and DC04 steels. Figure 9 shows the predicted thickness of the intermetallic layer, compared with experimental data at a number of locations from the center (assumed symmetrical). The model shows a small peak in layer thickness away from the weld center, though not as pronounced as in the experiments. This peak reflects the higher peak temperatures away from the center line (as shown in Fig. 8). The microstructural reactions are sensitive to temperature, and thus to the accuracy of the thermal model. To illustrate this sensitivity, the predictions were
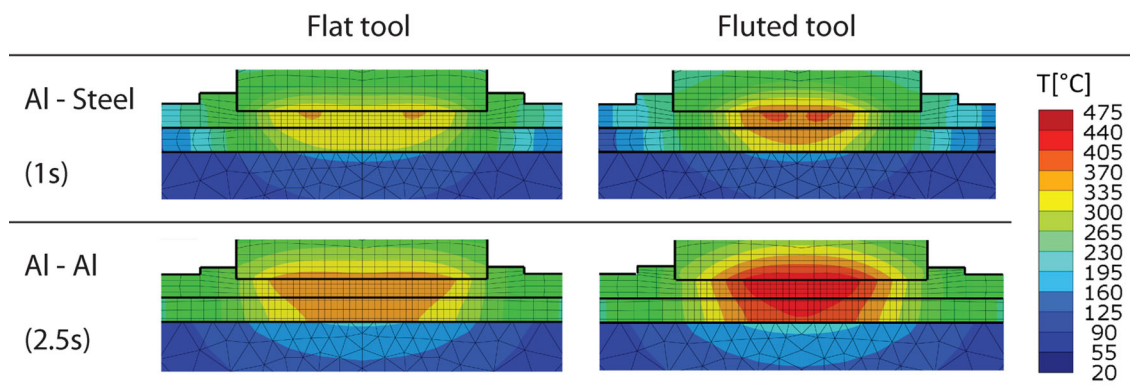


**Fig. 8** Predicted temperature distributions after 1.0 and 2.5 s dwell at the weld plane of symmetry for Al 6111-Al 6111 and Al 6111-DC04 welds, with flat and fluted tools
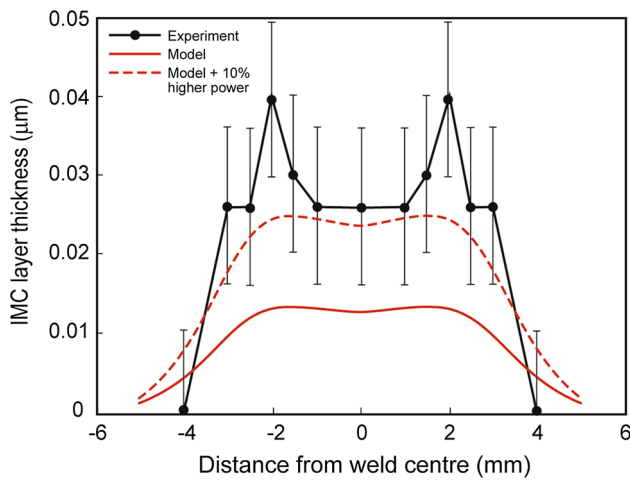
**Fig. 9** Thickness of the intermetallic layer at the interface for a 1s Al-steel weld with a flat tool—experimental data, and predictions using the calibrated thermal model with the nominal power input, and with an increase of 10% in power

repeated with an (arbitrary) increase in applied power of 10%, which is a reasonable upper limit on the combined inaccuracies of model calibration to thermocouple data, particularly for a weld of a duration of only 1 s. Figure 9 shows the prediction with this increase in power, which leads to roughly double the thickness of IMC layer, and a closer quantitative agreement with the experimental data. The model is therefore able to capture the interface reaction in a first-order way, but the analysis highlights the difficulty of making reliable quantitative predictions for this sort of problem in welding.

# 6. Microstructure and Hardness Evolution in Welding of AA6111

Studies of welding of heat-treatable aluminum alloys commonly measure the hardness profile across the weld, as an indicator of other mechanical properties (notably yield stress). There are many examples in the literature for friction stir spot welding (Ref 2, 5, 6, 33, 51) and for friction stir welding (Ref 52-56). Hardness also provides a valuable simple tool for tracking microstructural evolution, without recourse to time-consuming microscopy (Ref 52-54). The changes in hardness in Al-6111 can be attributed to dissolution and reprecipitation of hardening phases, with a secondary contribution from dislocation hardening in the thermomechanically affected zone (TMAZ) (Ref 57, 58). Loss of precipitation strengthening immediately after welding may be due to either precipitate coarsening or dissolution. These can be distinguished by measuring the hardness after subsequent natural aging, since only dissolution into solid solution can lead to subsequent natural aging. And in practical terms, the naturally aged state is the condition in which the weld would be used.

## 6.1 FSSW of Al-6111

Figure 10 shows the as-welded and naturally aged hardness profiles at mid-thickness of the upper sheet in Al-6111 FSSW, for each of two welding times. The hardness profiles should be
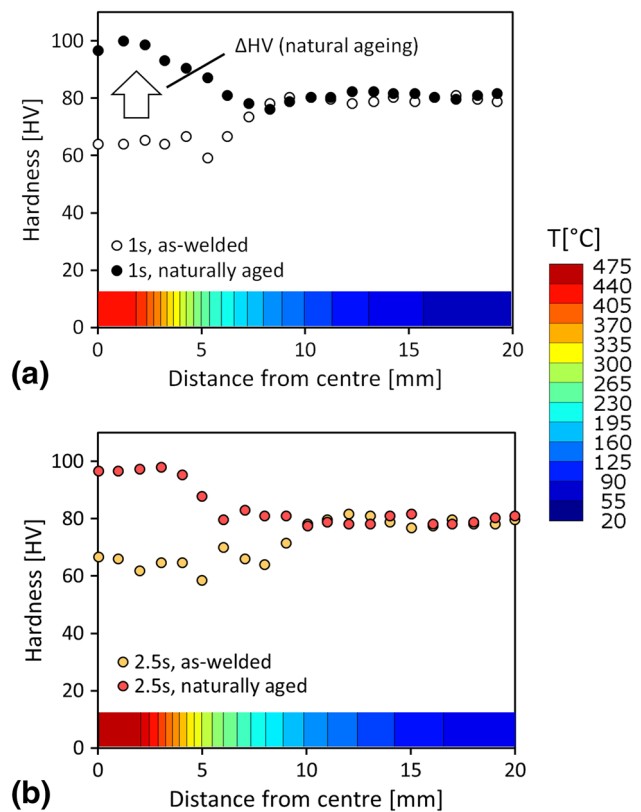


**Fig. 10** Hardness profiles at mid-thickness of the upper sheet in (a) 1s and (b) 2.5 s Al 6111-Al 6111 welds made with a fluted tool, both as-welded and after 3 months of natural aging [data from (Ref 5)].The corresponding predicted peak temperature distributions are superimposed below

symmetrical in FSSW, so to reduce the scatter the experimental hardness data from both sides of the center line of a given weld have been averaged (where available), and plotted as a half-profile in Fig. 10. In the as-welded condition, both exhibit the classical profile, commonly observed in both FSSW and FSW of heat-treatable Al alloys, with a heat-affected zone (HAZ) showing a minimum plateau in hardness extending some distance from the weld center. Natural aging leads to strength recovery across the entire HAZ, with the greatest increase occurring where the as-welded hardness was the lowest. Peak temperature predictions are superimposed below the hardness profiles, using the calibrated thermal model in each case.

The age-hardening behavior of quaternary Al-Mg-Si-Cu alloy AA6111 is complex, involving multiple metastable hardening phases, as precursors to the equilibrium phases β ($Mg_2Si$) and Q ($Al_4Cu_2Mg_8Si_7$) (Ref 59). Nonetheless, a simplified interpretation of the dominant softening and natural aging responses can be inferred from the behavior of welded 6000 series alloys in the literature.

In the initial condition, the Al-6111 is in a naturally aged T4 temper. The hardening phases in this temper will readily not only dissolve above their solvus temperature, but may also reprecipitate as other metastable phases. Depending on the thermal cycle imposed, a partial or complete supersaturated solid solution may be retained after welding. The only change in hardness that can occur during subsequent natural aging is reprecipitation of any available solute into the same phase as was initially responsible

for the T4 strength. The maximum possible recovery in strength by post-weld natural aging occurs where there has been full dissolution of the initial precipitates. This corresponds to the central plateau in hardness in Fig. 10, extending approximately 5-7 mm from the weld centerline, where the peak temperature exceeded roughly 300 °C. Note however that the post-weld naturally aged hardness exceeds that of the as-received sheet. This difference is attributed to dislocation hardening due to plastic deformation of the TMAZ. It is assumed that the dislocation hardening makes the same contribution in both the as-welded and naturally aged conditions, i.e., both profiles are a linear sum of two independent hardness contributions, with only the precipitation hardening changing.

The outer limit of the HAZ is at a distance of 7.5-10 mm from the center (depending on the weld time), where the peak temperature was roughly 150 °C. Between 150 and 300 °C, the as-welded hardness ramps downwards to its minimum as-welded value, indicating partial dissolution of the hardening precipitates. Over the same region, the naturally aged hardness ramps up to its maximum plateau value. What is most revealing therefore is to consider the *change* in hardness between the two, by subtracting one profile from the other. This hardness increment is directly related to the degree of solute supersaturation after welding. Furthermore, while the extent of dissolution depends on the whole thermal cycle, a first indicator of the kinetic strength of the cycle is given simply by the peak temperature. Hence the change in hardness has been cross-plotted against the peak temperature at each location, using the thermal model for each of the two welds in Fig. 10.

Figure 11 shows the difference between the smoothed hardness profiles in the as-welded and naturally aged conditions (black curves), as a function of predicted peak temperature during welding. The profiles for the two welds have a similar form, showing uniform maximum hardness change above 300 °C, and no change (outside the HAZ) below 150 °C. Between these temperatures, the hardness ramps up to the plateau value. Both profiles show a secondary maximum and minimum in this temperature interval. Profiles of exactly the
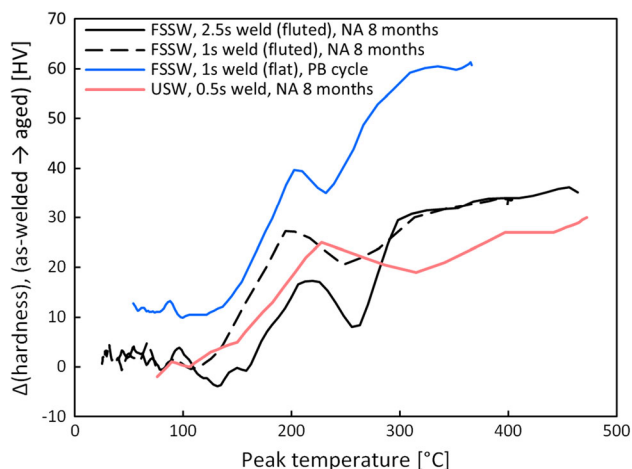
same shape have been seen in 2024-T3, subjected to isothermal holds of a few seconds duration and subsequently naturally aged (Ref 60). In 2024, this was attributed to partial precipitation of another hardening phase, reducing the solute available for natural aging. The same may be the case in 6111-T4, but this requires more detailed study.

The analysis is clearly approximate, given the uncertainty in temperature prediction in the model (of order 20-30 °C), and the smoothing of multiple hardness profiles. Nonetheless, the results suggest that there is a characteristic pattern in the hardness change during natural aging, as a function of peak temperature. From these results on 6111-T4, and the previous work on 2024-T3, it is apparent that the change in hardness after welding also depends on the weld duration, for an intermediate range of temperatures.

Further evidence is obtained by superimposing the corresponding data for a 1s FSSW of Al-6111 which was subjected to an elevated temperature artificial aging cycle at 180 °C after welding (corresponding to the paint-bake treatment used in the automotive industry). The blue curve in Fig. 11 shows that the profile is similar in form, but with a proportionately greater change in hardness throughout. This is consistent with the same initial supersaturation of solute (rising from zero below 150 °C, to 100% above 300 °C) being converted into more effective hardening phases by the elevated temperature heat treatment. Note that the secondary maximum and minimum in the profile at around 200 °C is replicated in this case.

### 6.2 Ultrasonic Welding of AA6111

The thermal cycles in friction stir spot welding have a duration of a few seconds. In these circumstances, it was shown above that the recovery in hardness due to post-weld natural aging correlates reasonably well with the peak welding temperature, for a given weld cycle time. To test this further, the same approach was applied to another solid-state welding process that takes a few seconds—ultrasonic welding (USW).

A 3D finite element thermal model of USW, presented by Jedrasiak et al. (Ref 62), was used to predict the thermal cycles (and thus peak temperatures) in a 0.5 s Al 6111 lap weld, produced experimentally by Chen et al. (Ref 61). The modeling approach for USW was similar, with the power profile as a function of time being inferred via thermocouple data. The welded joints were sectioned vertically through the center, parallel to the direction of vibration. Hardness profiles were made at mid-thickness of the top sheet, immediately after welding, and after natural aging for 8 months. The change in hardness as a function of position was determined from the profiles, and cross-plotted with the corresponding predicted peak temperature—see Fig. 11.

Given the completely different welding process and thermal model, and the scatter in the experimental data, the profiles for USW and FSSW are remarkably similar in form. The outer limit to the HAZ in USW also occurs at a peak temperature around 150 °C, with a comparable maximum hardness recovery at the highest weld temperatures. The ramp in hardness shows a weaker intermediate maximum and minimum around 250-300 °C. The degree of consistency suggests that simple semi-empirical correlations could be derived for a given alloy, between post-weld hardness and the corresponding peak temperatures and durations of the weld thermal cycles, derived from numerical models.



**Fig. 11** Increase in hardness from as-welded to post-weld aged state, against predicted peak temperature, for positions across the welds at mid-thickness of the upper Al 6111 sheet (three FSSW and one USW). Weld times, FSSW tools, and post-weld heat treatments as shown (NA, naturally aged; PB, paint bake). (Hardness data from Ref 5, 48, 61)

# 7. Conclusions

A thermal finite element model of friction stir spot welding of aluminum to aluminum, and aluminum to steel, was successfully developed for flat and fluted tools. The heat generation rate as a function of time, $q(t)$, was calibrated empirically to fit the temperature histories for selected welds. The radial distribution of heat generation was found to be dependent on the profiling of the tool. The calibrated model was applied to study two important microstructural changes in FSSW of aluminum.

Firstly, the thermal histories were combined with a microstructural model for the formation of intermetallic compounds at the interface in an Al 6111-steel weld. The models gave a reasonable quantitative prediction of the radial variation of the thickness of the intermetallic layer. The strong sensitivity of the microstructural results to uncertainty in the temperature history was demonstrated.

Secondly, the evolution of post-weld hardness of FSSW Al 6111 was studied. The recovery in hardness by post-weld natural aging was found to correlate systematically with the predicted peak temperature. A similar analysis was applied to ultrasonic welds in Al 6111, using a previously published thermal model. This confirmed that, for a given duration of thermal cycle, the relationship was characteristic of the alloy, and was independent of the welding process.

## References

1. J. Robson, A. Panteli, and P.B. Prangnell, Modelling Intermetallic Phase Formation in Dissimilar Metal Ultrasonic Welding of Aluminium and Magnesium Alloys, *Sci. Technol. Weld. Join.*, 2012, **17**(6), p 447–453
2. D. Bakavos and P.B. Prangnell, The Effect of Reduced or Zero Pin Length and Anvil Insulation on Friction Stir Spot Welding Thin Gauge 6111 Automotive Sheet, *Sci. Technol. Weld. Join.*, 2009, **14**, p 443–456
3. Y. Chen, H. Farid, and P. Prangnell, Feasibility Study of Short Cycle Time Friction Stir Spot Welding Thin Sheet Al to Ungalvanised and Galvanized Steel, *8th International Symposium on Friction Stir Welding*, Timmendorfer Strand, Lübeck, May 18–20, 2010
4. P.B. Prangnell, and D. Bakavos, Novel Approaches to Friction Spot Welding Thin Aluminium Automotive Sheet, *THERMEC 2009, PTS 1-4*, 2010, **1237–1242**(1–4), p 638–642
5. D. Bakavos, Y.C. Chen, L. Babout, and P.B. Prangnell, Material Interactions in a Novel Pinless Tool Approach to Friction Stir Spot Welding Thin Aluminum Sheet, *Metall. Mater. Trans. A*, 2011, **42A**(5), p 1266–1282
6. Y.C. Chen, S.F. Liu, D. Bakavos, and P.B. Prangnell, The Effect of a Paint Bake Treatment on Joint Performance in Friction Stir Spot Welding AA6111-T4 Sheet Using a Pinless Tool, *Mater. Chem. Phys.*, 2013, **141**(2–3), p 768–775
7. Y. Uematsu, K. Tokaji, Y. Tozaki, T. Kurita, and S. Murata, Effect of Re-filling Probe Hole on Tensile Failure and Fatigue Behaviour of Friction Stir Spot Welded Joints in Al-Mg-Si Alloy, *Int. J. Fatigue*, 2008, **30**(10–11), p 1956–1966
8. PSu Gerlich and T.H. North, Peak Temperatures and Microstructures in Aluminium and Magnesium Alloy Friction Stir Spot Welds, *Sci. Technol. Weld. Join.*, 2005, **10**(6), p 647–652
9. A. Gerlich, P. Su, and T.H. North, Tool Penetration During Friction Stir Spot Welding of Al and Mg Alloys, *J. Mater. Sci.*, 2005, **40**(24), p 6473–6481
10. A. Gerlich, G. Avramovic-Cingara, and T.H. North, Stir Zone Microstructure and Strain Rate During Al 7075-T6 Friction Stir Spot Welding, *Metall. Mater. Trans. A*, 2006, **37**(9), p 2773–2786
11. M. Yamamoto, A. Gerlich, T.H. North, and K. Shinozaki, Mechanism of Cracking in AZ91 Friction Stir Spot Welds, *Sci. Technol. Weld. Join.*, 2007, **12**(3), p 208–216
12. M. Gerlich, T.H. Yamamoto, and T.H. North, Local Melting and Cracking in Al 7075-T6 and Al 2024-T3 Friction Stir Spot Welds, *Sci. Technol. Weld. Join.*, 2007, **12**(6), p 472–480
13. P. Su, A. Gerlich, M. Yamamoto, and T.H. North, Formation and Retention of Local Melted Films in AZ91 Friction Stir Spot Welds, *J. Mater. Sci.*, 2007, **42**(24), p 9954–9965
14. A. Oosterkamp, L.D. Oosterkamp, and A. Nordeide, 'Kissing Bond' Phenomena in Solid-State Welds of Aluminum Alloys, *Weld. J.*, 2004, **83**(8), p 225S–231S
15. Y.S. Sato, H. Takauchi, S.H.C. Park, and H. Kokawa, Characteristics of the Kissing-Bond in Friction Stir Welded Al Alloy 1050, *Mat. Sci. Eng. A Struct.*, 2005, **405**(1–2), p 333–338
16. P. Su, A. Gerlich, T.H. North, and G.J. Bendzsak, Intermixing in Dissimilar Friction Stir Spot Welds, *Metall. Mater. Trans. A*, 2007, **38**(3), p 584–595
17. D. Kim, H. Badarinarayan, I. Ryu, J.H. Kim, C. Kim, K. Okamoto, R.H. Wagoner, and K. Chung, Numerical Simulation of Friction Stir Welding Process, *Int. J. Mater. Form.*, 2009, **2**, p 383–386
18. D. Kim, H. Badarinarayan, I. Ryu, J.H. Kim, C. Kim, K. Okamoto, R.H. Wagoner, and K. Chung, Numerical Simulation of Friction Stir Spot Welding Process For Aluminum Alloys, *Met. Mater. Int.*, 2010, **16**(2), p 323–332
19. C.D. Cox, B.T. Gibson, D.R. DeLapp, A.M. Strauss, and G.E. Cook, A method for double-sided friction stir spot welding, *J. Manuf. Process.*, 2014, **16**(2), p 241–247
20. C.D. Cox, J.R. Aguilar, M.C. Ballun, A.M. Strauss, and G.E. Cook, The Application of a Pinless Tool in Friction Stir Spot Welding: An Experimental and Numerical Study, *Proc. Inst. Mech. Eng. D J. Aut.*, 2010, **16**(2), p 323–332
21. S. Hirasawa, H. Badarinarayan, K. Okamoto, T. Tomimura, and T. Kawanami, Analysis of Effect of Tool Geometry on Plastic Flow During Friction Stir Spot Welding Using Particle Method, *J. Mater. Process. Tech.*, 2010, **210**(11), p 1455–1463
22. G. D'Urso, Thermo-Mechanical Characterization of Friction Stir Spot Welded AA6060 Sheets: Experimental and FEM Analysis, *J. Manuf. Process.*, 2015, **17**, p 108–119
23. Z. Gao, J.T. Niu, F. Krumphals, N. Enzinger, S. Mitsche, and C. Sommitsch, FE Modelling of Microstructure Evolution During Friction Stir Spot Welding in AA6082-T6, *Weld. World*, 2013, **57**(6), p 895–902
24. P. Lacki, Z. Kucharczyk, R.E. Sliwa, and T. Galaczynski, Effect of Tool Shape on Temperature Field in Friction Stir Spot Welding, *Arch. Metall. Mater.*, 2013, **58**(2), p 595–599
25. Z. Gao, F. Krumphals, P. Sherstnev, N. Enzinger, J.T. Niu, and C. Sommitsch, Analysis of Plastic Flow During Friction Stir Spot Welding Using Finite Element Modelling, *Material Forming: Esaform, Pts 1 & 2*, 2012, **504–506**, p 419–424
26. M. Miles, U. Karki, and Y. Hovanski, Temperature and Material Flow Prediction in Friction-Stir Spot Welding of Advanced High-Strength Steel, *JOM J. Miner. Met. Mater. Soc.*, 2014, **66**(10), p 2130–2136
27. S. Mandal, J. Rice, and A.A. Elmustafa, Experimental and Numerical Investigation of the Plunge Stage in Friction Stir Welding, *J. Mater. Process. Technol.*, 2008, **203**(1–3), p 411–419

28. K.H. Muci-Kuchler, S. Kalagara, and W.J. Arbegast, Simulation of a Refill Friction Stir Spot Welding Process Using a Fully Coupled Thermo-Mechanical FEM Model, *J. Manuf. Sci. Eng. T. ASME*, 2010, **132**(1), p 014503:1–5

29. S.U. Khosa, T. Weinberger, and N. Enzinger, Thermo-Mechanical Investigations During Friction Stir Spot Welding (FSSW) of AA6082-T6, *Weld. World*, 2010, **54**(5–6), p R134–R146

30. M. Awang and V.H. Mucino, Energy Generation during Friction Stir Spot Welding (FSSW) of Al 6061-T6 Plates, *Mater. Manuf. Process.*, 2010, **25**(1–3), p 167–174

31. B. Li and H. Kang, Temperature Distribution During Friction Stir Spot Welding of Magnesium Alloy AM60B, *J Test. Eval.*, 2011, **39**(1), p 1–9

32. A. Reilly, H.R. Shercliff, Y. Chen, and P.B. Prangnell, Modelling and Visualisation of Material Flow in Friction Stir Spot Welding, *J. Mater. Process. Technol.*, 2015 (in press)

33. Y.C. Chen, and P.B. Prangnell, Interface Structure and Bonding in Rapid Dissimilar FSSW of Al to Steel Automotive Sheet, *Proceedings of the 13th International Conference on Aluminium Alloys: ICAA 13*, Pittsburgh, PA, 2012

34. S.K. Khanna, X. Long, W.D. Porter, H. Wang, C.K. Liu, M. Radovic, and E. Lara-Curzio, Residual Stresses in Spot Welded New Generation Aluminium Alloys: Part A: Thermophysical and Thermomechanical Properties of 6111 and 5754 Aluminium Alloys, *Sci. Technol. Weld. Join.*, 2005, **10**(1), p 82–87

35. V. Kodur, S. Kand, and W. Khaliq, Effect of Temperature on Thermal and Mechanical Properties of Steel Bolts, *J. Mater. Civil Eng.*, 2012, **24**(6), p 765–774

36. E. Zolti, Comparative Review and Interim Data Base of Candidate Structural Materials. Elementary Tailored Martensitic Steel. SEAFP/R-M4/1, 1992

37. I.R. Choi, K.S. Chung, and D.H. Kim, Thermal and Mechanical Properties of High-Strength Structural Steel HSA800 at Elevated Temperatures, *Mater. Design*, 2014, **63**, p 544–551

38. M.M. Yovanovich, Four Decades of Research on Thermal Contact, Gap, and Joint Resistance in Microelectronics, *IEEE Trans. Compon. Packag. Technol.*, 2005, **28**(2), p 182–206

39. A. Reilly, H.R. Shercliff, G.J. McShane, Y. Chen, and P.B. Prangnell, Novel Approaches to Modelling Metal Flow in Friction Stir Spot Welding, *10th International Seminar on Numerical Analysis of Weldability*, Graz, 2012

40. S. Fukumoto, H. Tsubakino, K. Okita, M. Aritoshi, and T. Tomita, Microstructure of Friction Weld Interface of 1050 Aluminium to Austenitic Stainless Steel, *Mater. Sci. Technol.*, 1998, **14**(4), p 333–338

41. S. Bozzi, A.L. Helbert-Etter, T. Baudin, B. Criqui, and J.G. Kerbiguet, Intermetallic Compounds in Al 6016/IF-Steel Friction Stir Spot Welds, *Mat. Sci. Eng. A Struct.*, 2010, **527**(16–17), p 4505–4509

42. M. Sahin, Joining of Stainless-Steel and Aluminium Materials by Friction Welding, *Int. J. Adv. Manuf. Technol.*, 2009, **41**(5–6), p 487–497

43. M. Yilmaz, M. Col, and M. Acet, Interface Properties of Aluminum/Steel Friction-Welded Components, *Mater. Charact.*, 2002, **49**(5), p 421–429

44. T. Tanaka, T. Morishige, and T. Hirata, Comprehensive Analysis of Joint Strength for Dissimilar Friction Stir Welds of Mild Steel to Aluminum Alloys, *Scr. Mater.*, 2009, **61**(7), p 756–759

45. B.S. Yilbaş, A.Z. Şahin, N. Kahraman, and A.Z. Al-Garni, Friction Welding of St-Al and Al-Cu Materials, *J. Mater. Process. Technol.*, 1995, **49**(3–4), p 431–443

46. T. Liyanage, J. Kilbourne, A.P. Gerlich, and T.H. North, Joint Formation in Dissimilar Al Alloy/Steel and Mg Alloy/Steel Friction Stir Spot Welds, *Sci. Technol. Weld. Join.*, 2009, **14**(6), p 500–508

47. L. Wang, Y. Wang, P.B. Prangnell, and J. Robson, Modeling of Intermetallic Compounds Growth Between Dissimilar Metals, *Metall. Mater. Trans. A*, 2015, **46**(9), p 4106–4114

48. L. Wang, Y. Wang, C. Zhang, L. Xu, J. Robson, and P.B. Prangnell, Controlling Interfacial Reaction During Dissimilar Metal Welding of Aluminium Alloys, *Mater. Sci. Forum*, 2014, **794–796**, p 416–421

49. H. Springer, A. Kostka, E.J. Payton, D. Raabe, A. Kaysser-Pyzalla, and G. Eggeler, On the Formation and Growth of Intermetallic Phases During Interdiffusion Between Low-Carbon Steel and Aluminum Alloys, *Acta Mater.*, 2001, **59**, p 1586–1600

50. M. Kajihara, Analysis of Kinetics of Reactive Diffusion in a Hypothetical Binary System, *Acta Mater.*, 2004, **52**, p 1193–1200

51. D.A. Wang and S.C. Lee, Microstructures and Failure Mechanisms of Friction Stir Spot Welds of Aluminum 6061-T6 Sheets, *J. Mater. Process. Technol.*, 2007, **168**(1–3), p 291–297

52. Y.S. Sato, H. Kokawa, M. Enomoto, and S. Jogan, Microstructural Evolution of 6063 Aluminum During Friction-Stir Welding, *Metall. Mater. Trans. A*, 1999, **30**(9), p 2429–2437

53. Ø. Frigaard, Ø. Grong, and O.T. Midling, A Process Model for Friction Stir Welding of Age Hardening Aluminum Alloys, *Metall. Mater. Trans. A*, 2001, **32**(5), p 1189–1200

54. Y.S. Sato, M. Urata, and H. Kokawa, Parameters Controlling Microstructure and Hardness During Friction-Stir Welding of Precipitation-Hardenable Aluminum Alloy 6063, *Metall. Mater. Trans. A*, 2002, **33**(3), p 625–635

55. Y.S. Sato, S.W.C. Park, and H. Kokawa, Microstructural Factors Governing Hardness in Friction-Stir Welds of Solid-Solution-Hardened Al Alloys, *Metall. Mater. Trans. A*, 2001, **32**(12), p 3033–3042

56. P.L. Threadgill, A.J. Leonard, H.R. Shercliff, and P.J. Withers, Friction Stir Welding of Aluminium Alloys, *Int. Mater. Rev.*, 2009, **54**(2), p 49–93

57. M.H. Farshidi, M. Kazeminezhad, and H. Miyamoto, On the Natural Aging Behavior of Aluminum 6061 Alloy After Severe Plastic Deformation, *Mat. Sci. Eng. A Struct.*, 2013, **580**, p 202–208

58. W. Woo, L. Balogh, T. Ungar, H. Choo, and Z. Feng, Grain Structure and Dislocation Density Measurements in a Friction-Stir Welded Aluminum Alloy Using X-ray Peak Profile Analysis, *Mat. Sci. Eng. A Struct.*, 2008, **498**(1–2), p 308–313

59. X. Wang, S. Esmaeili, and D.J. Lloyd, The Sequence of Precipitation in the Al-Mg-Si-Cu Alloy AA6111, *Metall. Mater. Trans. A*, 2006, **37A**(9), p 2691–2699

60. H.R. Shercliff, M.J. Russell, A.D. Taylor, and T.L. Dickerson, Microstructural Modelling in Friction Stir Welding of 2000 Series Aluminium Alloys, *Mécanique et Industries*, 2005, **6**, p 25–35

61. Y.C. Chen, D. Bakavos, A. Gholinia, and P.B. Prangnell, HAZ development and accelerated post-weld natural ageing in ultrasonic spot welding aluminium 6111-T4 automotive sheet, *Acta Mater.*, 2012, **60**(6–7), p 2816–2828

62. P. Jedrasiak, H.R. Shercliff, Y.C. Chen, L. Wang, P.B. Prangnell, and J. Robson, Modeling of the Thermal Field in Dissimilar Alloy Ultrasonic Welding, *J. Mater. Eng. Perform.*, 2015, **24**(2), p 799–807